Analyzing the Inundation Pattern of the Poyang Lake Floodplain by Passive Microwave Data

HAOLU SHANG

State Key Laboratory of Remote Sensing Science, Institute of Remote Sensing and Digital Earth, Chinese Academy of Sciences, Beijing, China, and Delft University of Technology, Delft, Netherlands

LI JIA

State Key Laboratory of Remote Sensing Science, Institute of Remote Sensing and Digital Earth, Chinese Academy of Sciences, Beijing, China

MASSIMO MENENTI

Delft University of Technology, Delft, Netherlands

ABSTRACT

The soil wetness condition is a useful indicator of inundation hazard in floodplains, such as the Poyang Lake floodplain. Special Sensor Microwave Imager (SSM/I) passive microwave data were used to monitor water-saturated soil and open water areas of the Poyang Lake floodplain from 2001 to 2008, capturing the inundation patterns of this area in space and time. The polarization difference brightness temperature (PDBT) at 37 GHz is sensitive to the water extension even under dense vegetation. The zero-order radiative transfer model was simplified to retrieve the vertical–horizontal (V–H)-polarized effective emissivity difference from the PDBT at 37 GHz. Vegetation fractional area and vegetation transmission function were derived from NDVI to represent the vegetation attenuation. This effective emissivity difference has a quasi-linear relationship with the fractional area of water-saturated soil and standing water, no matter the frequency. Using the multifrequency-polarization surface emission (Q_p) model and the Dobson model of the soil–water mixture, the two segments of this relationship were combined into a quasi-linear model. Comparing the retrieved water-saturated soil and standing water area of Poyang Lake with the lake area obtained from the MODIS and synthetic aperture radar (SAR) image at higher spatial resolution, the calculations show a good fit with the MODIS and SAR data, with $R^2 = 0.7664$ and relative RMSE = 17.74%. The cross-correlation analysis shows that the Poyang Lake extension fluctuates with a 5-day time lag with the upstream land area of water-saturated soil and standing water. Since the closure of the Three Gorges Dam, this relationship is more evident.

1. Introduction

The soil wetness condition is a very important factor to describe the regional soil water-storage capacity, which determines the relative magnitude of surface runoff from precipitation. Thus, for hydrological applications, especially flood simulation and early warning, the soil wetness condition is a very critical variable.

However, it is difficult to measure the regional soil wetness condition by field measurements. A passive microwave radiometer at C or L band can provide soil moisture over large regions, but only from the topsoil down to a certain depth, which is determined by the wavelength. Because of the shallow soil layer sensed at 37 GHz (detected soil depth is around 0.8 mm), when this layer is water saturated, additional water will become vertical and horizontal water flow, or standing water after the deep soil layers are saturated. We could then consider the fractional area of water-saturated topsoil and standing water as an indicator of the residual water-storage capacity of the whole region. The

Corresponding author address: Li Jia, Institute of Remote Sensing and Digital Earth, Chinese Academy of Sciences, Datun Road Nr. 20, Beijing 100101, China.
E-mail: jiali@radi.ac.cn

surface runoff could be estimated based on that. In this paper, we retrieved the fractional area of water-saturated soil (WSS) and standing water from the polarization difference brightness temperature (PDBT) at 37 GHz in order to study the inundation pattern of large floodplains by satellite microwave observations.

The PDBT at 37 GHz is determined by the land surface temperature, the soil's polarized effective emissivity difference (PEED), and vegetation transmission. The open water fractional area for a densely vegetated floodplain in South America has been retrieved from the PDBT (Choudhury 1989; Hamilton et al. 1996; Sippel et al. 1994, 1998), under the assumption that the PDBT of dry soil and open water is constant in forest regions. This approach is only applicable for year-round green areas in South America, because of the relatively small temporal variability of land surface temperature and large and consistent attenuation by the vegetation canopy. To obtain the fractional area of WSS and standing water for seasonal vegetation–covered areas in temperate zones, we simplified the zero-order radiative transfer model (Kirdiashev et al. 1979; Wigneron et al. 1993) to retrieve the polarized effective emissivity difference from PDBT. The soil water saturation has a quasi-linear relationship with its PEED. We found that the fractional area of WSS and standing water can be represented by the soil water saturation, taking the spatial heterogeneity into account. Thus, this fractional area can be estimated from the PDBT at 37 GHz.

The dominant parameter of the zero-order radiative transfer model is the vegetation optical thickness. A lot of work has been done to parameterize it from different satellite observations, such as microwave vegetation index (Shi et al. 2008), leaf area index (Wen et al. 2003), and normalized difference vegetation index (NDVI) (Gao et al. 2004). Previous work assumed that the area is fully covered by vegetation. However, the vegetation fractional cover is also variable. For example, a wetland near a lake is highly influenced by the water extension and shows seasonal changes in the dry and wet seasons. The vegetation fractional area can be estimated from NDVI using a linear function, which we add into the radiative transfer model. The relationship between NDVI and PDBT at the monthly scale has been studied extensively for semiarid vegetation, forest, and grasslands (Choudhury 1989, 1991; Choudhury and Tucker 1987; Choudhury et al. 1990). In semiarid areas, the time series of PDBT is synchronous with NDVI at opposite trends. This suggests that when soil moisture is rather stable, attenuation by vegetation can be obtained from NDVI. We will develop this concept later.

The relationship between the soil PEED and the degree of soil water saturation is the bridge connecting the

satellite observations with the WSS and standing water area. This PEED is determined by the dielectric constant of the soil–water mixture. Both physical and empirical models have been proposed to model this, such as the Dobson model (Dobson et al. 1985) and the Wang–Schmugge model (Wang and Schmugge 1980). The quasi-linear relationship between the degree of soil water saturation and the PEED was first observed by De Ridder (2000) at 19 GHz by simulating the smooth surface soil emissivity with the Wang–Schmugge model. But, the dielectric constant of a soil–water mixture is frequency dependent. Simulated soil emissivity will also be different between models. Thus, we need to validate the quasi-linear relationship at 37 GHz and the consistency of this relationship across models.

Because of the revisit frequency and swath width of microwave radiometers on polar-orbiting satellites, time series of passive microwave data have gaps of 3–5 days. To make a consistent daily time series, we need some statistical methods, such as a moving window filter, to fill these observation gaps. In addition, the effects of raindrops on microwave observations at 37 GHz are not negligible. Geolocation and resampling introduce errors in the conversion from swath brightness temperature (BT) to the gridded data. Erroneous observations therefore need to be identified and removed. In this case, we applied the Harmonic Analysis of Time Series (HANTS) algorithm (Menenti et al. 1993; Roerink et al. 2000; Verhoef 1996) to fill gaps and remove noisy samples. The fast Fourier transform (FFT) and HANTS have been developed and applied to time series of satellite observations, for example, NDVI and land surface temperature, to study vegetation phenology and land surface climate (Alfieri et al. 2013; Jia et al. 2011; Julien et al. 2006; Menenti et al. 1993, 2010; Moody and Johnson 2001; Roerink et al. 2000, 2003; Verhoef 1996). Different from the FFT by using all observations regardless of quality, the HANTS identifies and removes outliers in data samples. We aimed at evaluating its applicability to satellite microwave radiometric data.

The objective of this paper is to study the inundation pattern in the up- and downstream area of the Poyang Lake floodplain in relation with the WSS and standing water area retrieved from passive microwave observations. Poyang Lake is the largest lake in the Yangtze River basin. As the major natural water reservoir of the Yangtze River basin, the inundation pattern of this floodplain has a significant influence on both local and downstream water resource management.

There are five sections in this paper: introduction, study area and dataset, methods, results, and conclusions. In the methods, the algorithm for retrieving the WSS and standing water area from the PDBT at 37 GHz
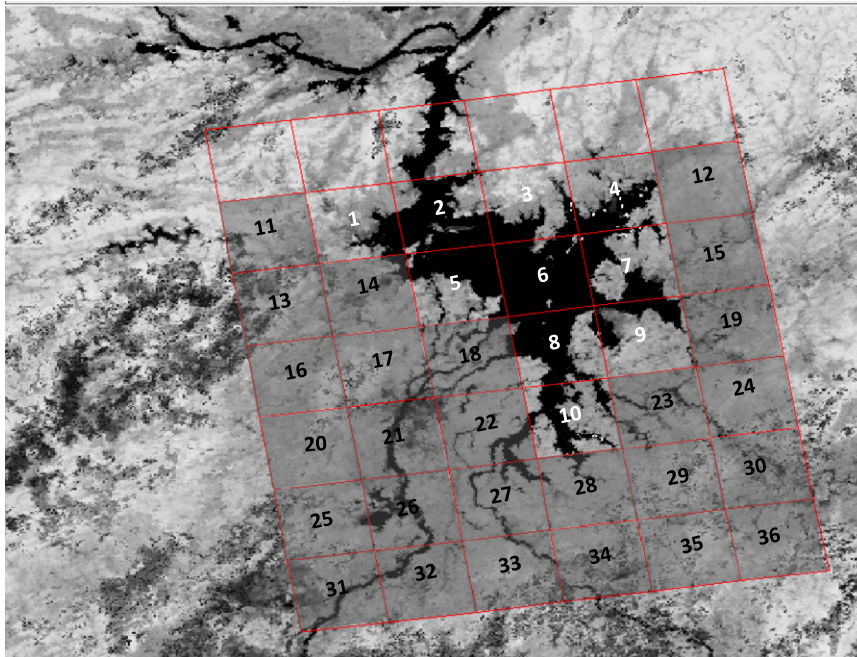
FIG. 1. The study area of Poyang Lake and its upstream area.

is developed. Then, we demonstrate the details of the algorithm from data procession to parameter derivation step by step. In the results, the preprocessed data are compared with the original data to show the improvement after gap filling and noise removal. After solving the parameter-derivation problems, the retrieved fractional area of the WSS and standing water of Poyang Lake area is compared with the lake area obtained from the Moderate Resolution Imaging Spectroradiometer (MODIS) and advanced synthetic aperture radar (ASAR) data.

2. Study area and dataset

The study area is the floodplain including Poyang Lake [see the squares in Fig. 1, which are the Equal-Area Scalable Earth Grid (EASE-Grid) with a spatial resolution of 25 km (Brodzik and Knowles 2002)]. It is the largest lake in the Yangtze River basin, located between 28.048° and 29.384°N and 115.444° and 117.007°E. There is a clear dry season from October to March, and the flooding season is from April to September. The low residual water-storage capacity of this floodplain was one of the major causes of the extreme flooding over the Yangtze River basin in 1998. Thus, it is chosen as our study area.

Currently, there are two sensors providing dual polarization measurements around 37 GHz: the Special Sensor Microwave Imager (SSM/I) and the Advanced Microwave Scanning Radiometer for EOS (AMSR-E). In this case, the SSM/I on board the Defense Meteorological Satellite Program (DMSP) *F13* satellite is used. It is a seven-channel, four-frequency radiometric system that has provided global observations at a constant angle of incidence of 51.2° since July 1987 (Hollinger et al. 1990). No data were acquired from 2 December 1987 to 12 January 1988 because of overheating of the sensor. The period of our study is from 2001 to 2008, to ensure that the observations by MODIS overlap with the enclosure of the Three Gorges Dam (in November 2002). The footprint of the 37-GHz observations is about 28 km × 37 km, with geolocation uncertainty of about 8 km. We used the data acquired at 0558:00 local time (LT). The AMSR-E on board the *Aqua* satellite measures radiation since May 2001 at six frequencies in the range of 6.9–89 GHz, all at dual polarization, with a constant angle of incidence of 55°. The 36.5-GHz data have a footprint of 14 km × 8 km and are acquired at 0130:00 LT. The SSM/I brightness temperature has been intercalibrated with that of AMSR-E, and both are registered into the EASE-Grid system. Thus, for the same pixel area, the time series of PDBT at similar frequencies (37 GHz for SSM/I and 36.5 GHz for AMSR-E) should have similar fluctuations. The PDBT time series of these two sensors are compared to validate the consistency, observation bias, and possible noise. The daily SSM/I and AMSR-E data gridded into the EASE-Grid (Brodzik and Knowles 2002) were

downloaded from the National Snow and Ice Data Center (NSIDC) (Armstrong et al. 1998). The Poyang Lake area covers 10 pixels of EASE-Grid data, as indicated in Fig. 1 by the white-numbered squares. The upstream area of the Poyang Lake covers the four major tributary river systems coming from the west, southwest, southeast, and east, and indicated in Fig. 1 by the gray-shaded squares with black numbers.

This study uses two MODIS data products: the MOD09A1 8-day composite surface reflectance data of MODIS bands 1–7, which are used in the calculation of vegetation fractional area and vegetation optical thickness; and the MOD13A2 16-day composite NDVI data, which are used to derive the relationship between NDVI and vegetation optical thickness. The spatial resolution of the reflectance dataset is 500 m, while the NDVI dataset is 1 km. Because of the nonlinear dependence of NDVI on red and near-infrared reflectance, these two bands will be averaged first over each EASE-Grid and then used to calculate its NDVI. MOD13A2 is used in the parameter derivation, mainly because of its high quality data. MOD09A1 is chosen from the best quality atmosphere condition during each 8-day measurement. MOD13A2 corrects the viewing angle difference based on MOD09A1; thus, large off-nadir and forward-scattering view angles and large solar zenith angles are avoided in MOD13A2.

3. Methods

The remote sensing data, that is, the MOD09A1 and SSM/I 37-GHz brightness temperature data, are used to retrieve the water-saturated soil and open water area. These data are first preprocessed to remove noise and daily gaps. The zero-order radiative transfer model is simplified, in order to use these processed remote sensing data to retrieve the surface PEED. A linear model is then developed to calculate the WSS and open water area from the PEED. The overview of the theory of our method is explained in section 3a, and the detailed explanation of each step is given in sections 3b–d.

a. Theory and flowchart of retrieving fractional area of WSS and standing water from passive microwave measurements

1) SIMPLIFIED RADIATIVE TRANSFER MODEL

Satellite microwave radiometers measure the radiance emitted by the land surface, such as soil, standing water, and snow. This radiance is determined by the surface temperature, surface emissivity, and surface roughness, and it is attenuated by the vegetation canopy

and atmosphere. The zero-order radiative transfer model is often used to describe the energy transfer from the land surface to the radiometer. We simplified this model to retrieve the PEED from the PDBT ΔT at 37 GHz as follows:

$$\Delta T = T_s \Delta \epsilon [(1 - f_{\text{veg}}) + f_{\text{veg}} \exp(-2\tau_0/\mu)], \quad (1)$$

where T_s is the surface brightness temperature; $\Delta \epsilon$ is PEED; f_{veg} is the vegetation fractional area; $\mu = \cos(\theta)$, where θ is zenith view angle; and τ_0 is the optical thickness of vegetation.

The single scatter albedo of the vegetation canopy at two polarizations is assumed to be the same. The apparent brightness temperature of the sky is negligible compared with the land surface temperature. Under the above two assumptions, we get Eq. (1) from the zero-order radiative transfer model.

2) LINEAR MODEL TO RETRIEVE FRACTIONAL AREA OF WSS AND STANDING WATER

Since the PEED is obtained from Eq. (1), the fractional area of WSS and standing water f_{ws} can be derived from the following linear equation:

$$f_{\text{ws}} = (\Delta \epsilon - \Delta \epsilon_{\text{dry}})/(\Delta \epsilon_{\text{sat}} - \Delta \epsilon_{\text{dry}}), \quad (2)$$

where $\Delta \epsilon_{\text{dry}}$ and $\Delta \epsilon_{\text{sat}}$ are the PEED of completely dry soil and water-saturated soil, respectively. Their derivation method will be discussed in section 3d. The variable $\Delta \epsilon_{\text{sat}}$ has the same value with that of water; thus, the fractional area in Eq. (2) represents the sum of the WSS and standing water.

Equation (2) is established based on the definition transform from the water saturation condition to the fractional area of WSS and standing water as follows:

$$f_{\text{ws}} = \sum_{i=1}^{n} (f_i W_i/W_{\text{sat},i}) = W_{r,s}/W_{\text{sat}}, \quad (3)$$

where f_i is the fractional area of the ith subpixel area with the volumetric soil moisture W_i ($\text{cm}^3\,\text{cm}^{-3}$) and the field capacity of this subpixel area $W_{\text{sat},i}$ ($\text{cm}^3\,\text{cm}^{-3}$); n is the number of the subpixel areas; $W_{r,s}$ ($\text{cm}^3\,\text{cm}^{-3}$) is the volumetric soil moisture of the whole pixel region; and W_{sat} ($\text{cm}^3\,\text{cm}^{-3}$) is the regional field capacity.

In Eq. (3), the spatial heterogeneity of the soil moisture in one pixel region is formulated by the field capacity of the subpixel area, which is determined by its soil texture. The regional water saturation condition is represented by the sum of its subregion conditions. The fractional area f_i and the water saturation condition of each subpixel $W_i/W_{\text{sat},i}$ in Eq. (3) are transformable to each other, because both can be taken as the weight
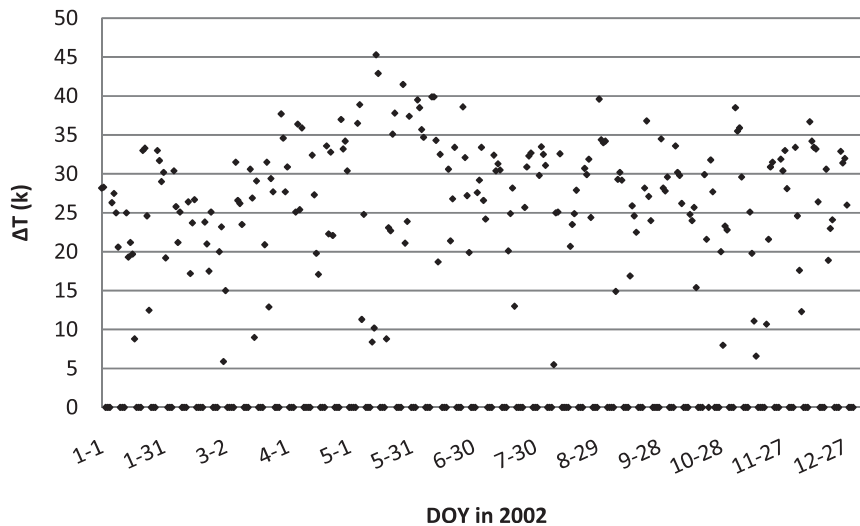
FIG. 2. Time series of raw PDBT (i.e., ΔT) data at one pixel of Poyang Lake for different days of the year (DOY) in 2002.

factor of the other. Thus, in Eq. (3), the fractional area of WSS and standing water has the same definition as the regional water saturation condition $W_{r,s}/W_{sat}$. According to De Ridder (2000), the regional water saturation condition could be derived from the PEED by a linear relationship, which we will discuss in section 3d.

3) OVERVIEW OF THE RETRIEVAL METHOD

The processing steps to retrieve the fractional area of the WSS and standing water are as follows:

1) Gap filling and noise removal. Preprocess the passive microwave data by moving filter and HANTS to obtain a daily noise-free estimation of the PDBT and vertical BT data at 37 GHz. Aggregate the MOD09A1 and preprocess the NDVI by HANTS to obtain daily noise-free NDVI data (see section 3b).
2) Retrieve the PEED. The parameters of the simplified radiative transfer model in Eq. (1) need to be derived from the satellite observations in order to retrieve the PEED. The land surface temperature can be derived from the vertical BT at 37 GHz, and the vegetation fractional area can be obtained from NDVI data. The derivation of the vegetation optical thickness from NDVI is discussed in detail in section 3c.
3) Retrieve the fractional area of the WSS and standing water. The parameters of the linear model in Eq. (2) need to be determined through the model simulation of soil–water mixture and surface roughness, because there are no field measurements for this area. Then, the fractional area of the WSS and standing water can be retrieved using Eq. (2) (see section 3d).

Besides the steps listed above, the FFT method is used to determine the major parameters used in HANTS (see

section 3b). To validate the frequency and model dependence of the parameters' derivation of Eq. (2), we used two soil–water mixture models, the Wang–Schmugge model and the Dobson model, to simulate the PEED at frequencies of 1.4, 19, and 37 GHz (see section 3c).

b. Gap filling and noise removal

To create a consistent time series of microwave data, erroneous observations need to be identified and removed and the gaps in the time series need to be filled.

First, we used a 10-day moving window filter to preprocess the time series of PDBT and vertically polarized BT. In each window, the maximum and minimum nonzero values were removed, and the average of the remaining values was the estimation of the central day. The window size was chosen according to the gap size in the time series (the gap size caused by the revisiting schedule is 3–5 days) and the need to retain a sufficient number of samples. The upper and lower envelopes of the time series are potential erroneous observations (larger scatter of the upper and lower envelope samples is shown in Fig. 2). Extremely low values are probably caused by the raindrops and wind. Besides those, the integration method used in the SSM/I EASE-Grid product introduces extremely high and extremely low values. That is because a weighted sum of the brightness temperature in each 4×4 array is used to represent the brightness temperature at its central location in the EASE-Grid products (Poe 1990). These weight factors are the description of the antenna pattern. Thus, nearby pixels will significantly influence the gridded data, with possible under- and overestimations of PDBT, so we removed the maximum and minimum value in the moving window.

TABLE 1. Duration of different stages (days) of rice growth cycle and their flooding condition.

Periods	Period of seeding establishment	Early period of tillering	Late period of tillering	Booting stage	Heading stage	Milk stage	Yellow ripening stage
Early rice	18	18	13	15	12	9	15
Late rice	6	18	14	21	11	12	26
Flooding condition	Flooded or early period is flooded, later period is drying	Flooded	Flooded or drying	Flooded	Flooded	Wet	Drying

However, when durative measurements are taken under precipitation, for example, during the rainy season, the filtered time series will be underestimated. To remove such noise in filtered time series, we applied the HANTS algorithm (Menenti et al. 1993; Roerink et al. 2000; Verhoef 1996). The main user-selectable parameters of the HANTS algorithm are the number of harmonics and their period, high/low outlier direction, valid data range, fit error tolerance, and degree of overdeterminedness [see Jia et al. (2011) and Roerink et al. (2000) for detailed information].

To determine the number and periods of the frequencies used in the HANTS algorithm, we have applied the FFT algorithm to 1-yr time series of both 37-GHz PDBT and vertical BT data. The components with the first three largest amplitudes were chosen for the three main land use types in the Poyang Lake floodplain—wetland, open water, and cropland. These components are enough to regress the upper envelope of the original time series (called a reconstruction). The precipitation-contaminated observations have lower values and thus are removed as outliers during the reconstruction. The HANTS algorithm was also applied to NDVI time series to obtain cloud-free daily NDVI. The number and periods of the dominant frequencies are determined in a similar way as above.

c. Parameter derivation of the simplified radiative transfer model

To calculate the fractional area of WSS and standing water using Eq. (1), land surface temperature, fractional vegetation area, and vegetation optical thickness need to be derived from satellite observations. The variable T_s can be obtained from the vertical BT $T_{B,37V}$ at 37 GHz (Holmes et al. 2009):

$$T_s = 1.11(T_{B,37V}) - 15.2. \quad (4)$$

The green vegetation fractional area f_{veg} can be estimated from NDVI as

$$f_{veg} = (NDVI - NDVI_{soil})/(NDVI_{veg} - NDVI_{soil}), \quad (5)$$

where $NDVI_{soil}$ is that of bare soil and $NDVI_{veg}$ is that at full vegetation cover. In this case, $NDVI_{soil}$ is set as

0 because of water-saturated soil. The $NDVI_{veg}$ of rice is set as 0.60, the same as that of shrubland.

The vegetation optical thickness is approximately a linear function of NDVI (van de Griend and Owe 1993). The opposite fluctuations of the time series of NDVI and PDBT in arid areas suggest that when the surface temperature and water saturation are constant, the ΔT changes because of vegetation transmission. To derive the vegetation optical thickness, we modified Eq. (1) as

$$\Delta T = \Delta T_s\{(1 - f_{veg}) + f_{veg}\exp[-A(NDVI)]\}, \quad (6)$$

where $\Delta T_s = T_s(\Delta\epsilon)$, which is the PDBT emitted from the land surface. In Eq. (6), the vegetation optical thickness is linearly determined by NDVI with a coefficient A. The angle of incidence is also contained in this coefficient. To simplify our process, we defined this exponential function in Eq. (6) as the vegetation transmission function (denoted as δ):

$$\delta = \exp[-A(NDVI)]. \quad (7)$$

So, in fact, we derive the vegetation transmission function of Eq. (7), instead of the vegetation optical thickness, from NDVI.

To determine A using Eq. (6), a set of observations where ΔT_s is constant and ΔT only changes with NDVI is necessary. Because f_{veg} can be obtained from NDVI using Eq. (5), the only undetermined parameters in Eq. (6) are two constants: ΔT_s and A. Thus, by regressing NDVI with its dependent variable ΔT using Eq. (6), we can derive A (see the equation in Fig. 6, described in greater detail below).

Flooded paddy fields fit this assumption very well. Paddy fields are flooded in specific periods of the growing season (as shown in Table 1). Normally, between two adjacent flooding periods, there is a long dry period. Thus, the irrigated paddy fields can be taken as flooded or water-saturated area and the unirrigated paddy fields can be taken as dry soil. The fractional area of paddy fields does not change year by year according to local statistical records, and rice growth demands a strict irrigation plan. This guarantees consistent PEED during the flooding periods. The land surface temperature is also constant in the early morning of the

flooding periods (SSM/I measures in the early morning) because of the relative high thermal capacity of water. Thus, ΔT_s (i.e., underneath the rice canopy) of the paddy fields can be taken as a constant during the flooding periods. Then, we can apply Eq. (6) on the coupled ΔT and NDVI observation to regress A.

d. Parameter derivation of the linear model

The linear model of Eq. (2) comes from the hypothesis that the regional water saturation condition is linearly related with the retrieved PEED as follows:

$$W_{r,s}/W_{sat} = (\Delta\epsilon - \Delta\epsilon_{dry})/(\Delta\epsilon_{sat} - \Delta\epsilon_{dry}). \quad (8)$$

This has been proven at 19 GHz by De Ridder (2000) using the Wang–Schmugge model (Wang and Schmugge 1980) to simulate the dielectric constant of soil–water mixture for a smooth surface. However, the dielectric constant of a soil–water mixture ϵ_v is frequency v dependent, and there are some other models available, such as the Dobson model (Dobson et al. 1985). In this case, both the Wang–Schmugge and the Dobson models are used to estimate the dielectric constant of soil–water mixture at frequencies of 1.4, 19, and 37 GHz. Then, the PEED of rough soil surface is calculated by the multifrequency-polarization surface emission (Q_p) model (Shi et al. 2005) as follows:

$$\Delta\epsilon = [1 - (Q_H + Q_V)][\Gamma_{s,s}(H, \theta, v) - \Gamma_{s,s}(V, \theta, v)], \quad (9)$$

where Q_H and Q_V are the surface roughness parameters for horizontal H and vertical V polarizations, respectively, at the angle of incidence θ. They can be obtained from the roughness property of the surface, named s/l, which is the ratio of RMS height s to correlation length l. Variables $\Gamma_{s,s}(H, \theta, v)$ and $\Gamma_{s,s}(V, \theta, v)$ are the reflectivity of a smooth surface for horizontal and vertical polarization, respectively, which is determined by the Fresnel equations:

$$\Gamma_{s,s}(H, \theta, v)$$
$$= \left| \left(\cos\theta - \sqrt{\epsilon_v - \sin^2\theta} \right) \Big/ \left(\cos\theta + \sqrt{\epsilon_v - \sin^2\theta} \right) \right|^2 \quad (10)$$

and

$$\Gamma_{s,s}(V, \theta, v)$$
$$= \left| \left(\epsilon_v \cos\theta - \sqrt{\epsilon_v - \sin^2\theta} \right) \Big/ \left(\epsilon_v \cos\theta + \sqrt{\epsilon_v - \sin^2\theta} \right) \right|^2. \quad (11)$$

The Dobson (Dobson et al. 1985) and the Wang–Schmugge (Wang and Schmugge 1980) models are used to calculate the dielectric constant of soil–water mixture at frequencies of 1.4, 19, and 37 GHz. The dominant

parameter of these two models is soil texture. A silt-loam soil was used in this numerical analysis with 13.5% clay and 30.6% sand, since it is the major soil type in the Poyang Lake area. Because of the calibration difficulty, the parameters of the Dobson model were not recalibrated while the parameters of the Wang–Schmugge model at 37 GHz were recalibrated by Calvet et al. (1995).

4. Results

a. Gap filling and noise removal on time series of PDBT

Our FFT analysis of the PDBT time series showed that there were eight dominant frequencies and that their corresponding periods were 365, 183, 122, 91, 73, 61, 46, and 30 days. The vertically polarized BT time series had exactly the same frequencies, according to their own FFT analysis. We set the other parameters required to apply the HANTS algorithm to the PDBT and vertical BT time series as follows:

- the direction of outliers was lower,
- the fit error tolerance was 1.5 K,
- the degree of overdeterminedness was 80, and
- the valid data ranges were 3–100 K for PDBT and 200–400 K for vertical BT.

The FFT analysis of NDVI time series showed that there were six frequencies and their corresponding periods were 365, 184, 123, 91, 74, and 61 days. The other parameters were set as follows:

- the direction of outliers was lower,
- the fit error tolerance was 0.05,
- the degree of overdeterminedness was 20, and
- the valid data range was 0–1.

The moving window–filtered brightness temperature data are the daily estimation. They follow the overall trend of the raw data in Fig. 3. The raw data time series in Fig. 3 show much scattering, while the moving window–filtered data give a much clearer trend of the time series.

The sharp sags of raw and filtered PDBT during the continuous rainfall is probably caused by the attenuation of raindrops as they occur at the same duration as the precipitation in Fig. 3. The HANTS algorithm throws out these relatively lower-valued samples as outliers. The upper envelope of the filtered time series is followed by the reconstruction time series. HANTS can work because the spatial heterogeneity slows the response of the regional soil moisture to precipitation. The time series of daily region-averaged soil moisture observed in Tibet is much smoother than that at hourly resolution, according to the field observations by Zhao et al. (2013).
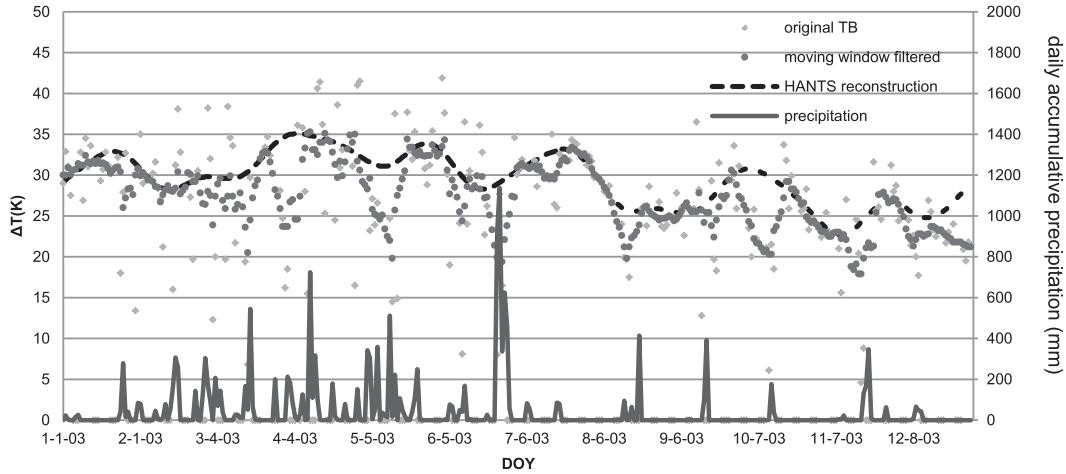
FIG. 3. Time series of raw PDBT (i.e., ΔT) data in 2003 averaged over the Poyang Lake area, after a 10-day moving filter and reconstructed with HANTS and daily precipitation.

b. Parameterization of the vegetation transmission function

To compare with the PDBT data, MOD13A2 NDVI data were aggregated to a 25 km × 25 km EASE-Grid, because the aggregation from NDVI and reflectance (MOD09A1) does not show large differences for the paddy fields (shown in Fig. 4), and the data quality of MOD13A2 is much better than MOD09A1 without sudden low values (cloud-contaminated samples) in the aggregated NDVI time series of MOD13A2. This consistency is only found for cropland area. For other land types with large spatial heterogeneity, NDVI data are calculated from the spatially aggregated reflectance data (MOD09A1).

During each rice cropping season in 2002 (one from April to July and the other from July to October, according to the NDVI time series of Fig. 5), there is a significant peak occurring in PDBT time series at its start time. This indicates the sowing time and the start of

irrigation of the paddy fields, since the PDBT increases with WSS and standing water area. The flood duration is about 50 days, as shown in Table 1. It covers several stages of rice phenology and includes three or four observations of the 16-day composite NDVI data. Since the irrigation schedule is similar among fields, the surface emittance and PDBT can be taken as constants during these 50 days at the observation time (early morning). Thus, the radiometer-measured PDBT is only affected by the vegetation fractional area and optical thickness. The vegetation fractional area can be calculated from NDVI using Eq. (5). The vegetation optical thickness, which describes the scattering and absorption of the surface emittance by vegetation, can be parameterized by NDVI using the vegetation transmission function of Eq. (7). The simplified radiative transfer model appears in Eq. (6) to clarify this.

To get sufficient observations to estimate the coefficients in Eq. (6), we chose NDVI data and corresponding average
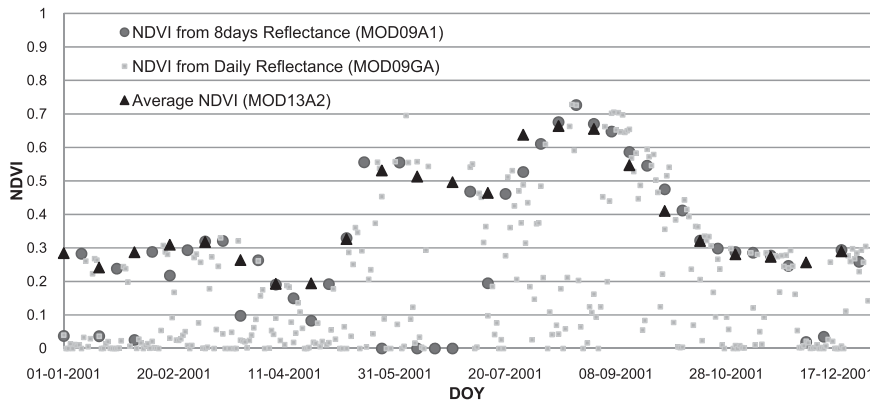

FIG. 4. Time series of spatially aggregated NDVI of paddy fields from MOD09A1, MOD09GA, and MOD13A2.
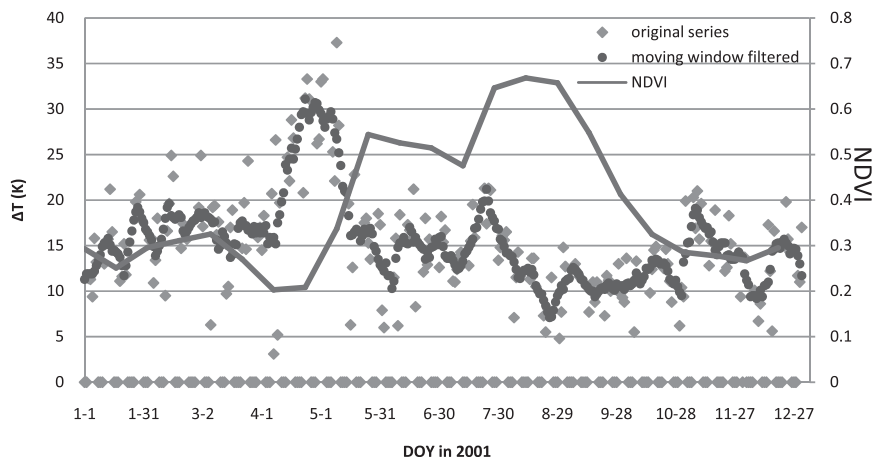
FIG. 5. Time series of original PDBT (i.e., ΔT) data, moving window–filtered PDBT, and NDVI at the paddy field in 2001.

PDBT data of one EASE-Grid pixel area (25 km × 25 km; centrally located at 28.3807°N, 115.8351°E) during the rice flooding periods from 2001 to 2003 (as shown in Fig. 6), since this area is almost entirely covered by paddy fields and the rice area in this region shows little variability during these 3 years according to local statistical records. By fitting the data points with Eq. (6), we get the regression equation as shown in Fig. 6: ΔT_s in Eq. (6) is 26.9 K and A is 1.231 79. Thus, the vegetation transmission function of Eq. (7) is

$$\delta = \exp[-1.23179(\text{NDVI})]. \qquad (12)$$

In this regression, we did not use Eq. (4) to calculate the land surface temperature, because the model uncertainty of Eq. (4) might be introduced into the derivation of the vegetation transmission function. The uncertainty of this regression is highly dependent on the vegetation fractional area. We compared the linear and quadratic model for deriving vegetation fractional area from NDVI. When the same setting of NDVI_veg and NDVI_soil as described in section 3b is used, the RMSE of our regression with the quadratic model is 3.2 K, higher than that in Fig. 6.

The parameter definition of vegetation fractional area model in Eq. (5) has little influence on this regression. We evaluated different settings of NDVI_soil (-0.05, 0, and 0.05), which is the major model uncertainty in Eq. (5). The RMSE of our regression only varies from 2.7 to 2.8 K. Because there is no field measurement of NDVI for flooded soil, which could have negative values close to water, we simply set $\text{NDVI}_\text{soil} = 0$.

c. Evaluation of the relationship between the emissivity difference and soil wetness

We modeled the smooth surface emissivity difference at 1.4, 19, and 37 GHz with both the Wang–Schmugge and the Dobson models, as shown in Fig. 7. Both model
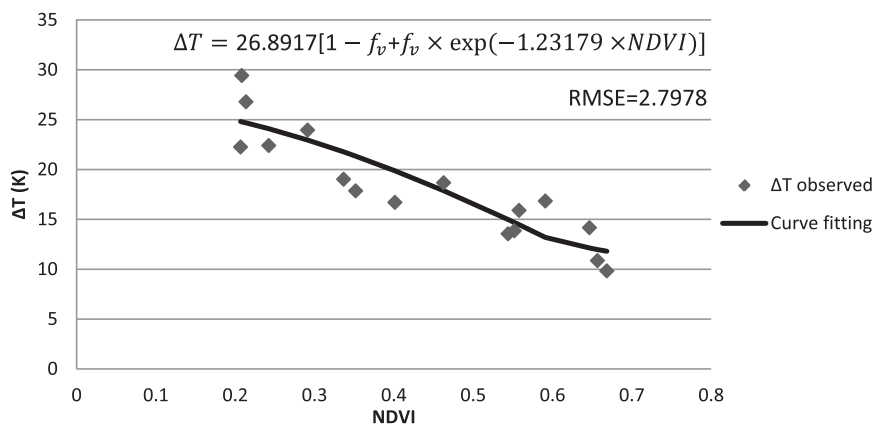

FIG. 6. Scatterplots of PDBT (i.e., ΔT) data and corresponding NDVI observations and the result of curve fitting.
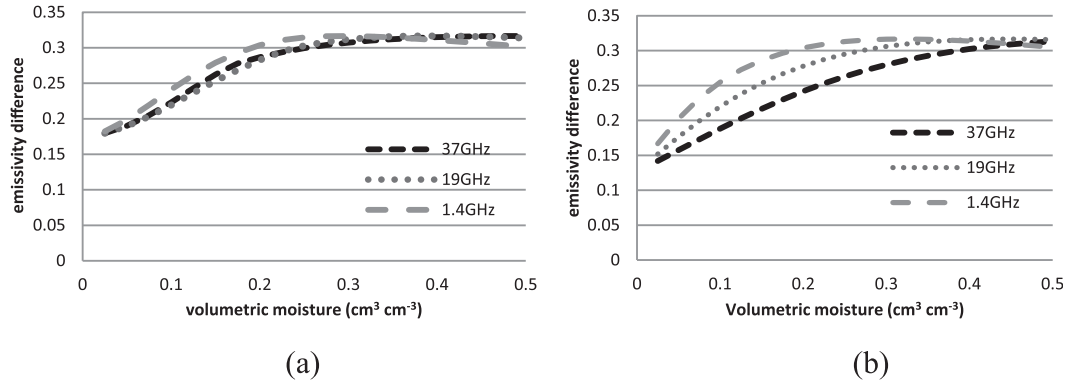
FIG. 7. Emissivity difference for silt-loam soil: (a) Wang–Schmugge and (b) Dobson models.

simulations show (Fig. 7) that a quasi-linear relationship exists at all frequencies, but with different slopes and interceptions. The Wang–Schmugge model gives a very similar slope at different frequencies: the emissivity difference increases from 0.17 with volumetric soil moisture, reaching a plateau at $\Delta\epsilon = 0.3$, when the volumetric soil moisture is close to $0.255\,\mathrm{cm}^3\,\mathrm{cm}^{-3}$ (Fig. 7a), which is the field capacity of the silt-loam soil (De Ridder 2000). The Dobson model simulation shows that the slope of the quasi-linear relationship is dependent on frequencies, while the plateau of $\Delta\epsilon$ has very similar values at all three frequencies (Fig. 7b). At 1.4 GHz, $\Delta\epsilon$ increases from 0.16 and reaches the plateau at $\Delta\epsilon = 0.3$ for a soil volumetric moisture close to $0.14\,\mathrm{cm}^3\,\mathrm{cm}^{-3}$. At 19 GHz, $\Delta\epsilon$ starts to increase at 0.15 and reaches the same plateau when the soil gets wetter than for 1.4 GHz, at a soil volumetric moisture around $0.26\,\mathrm{cm}^3\,\mathrm{cm}^{-3}$. At 37 GHz, it increases from an even lower $\Delta\epsilon$ around 0.14 and reaches the plateau when the soil moisture is close to $0.5\,\mathrm{cm}^3\,\mathrm{cm}^{-3}$.

The Dobson model suggests that at the higher frequency the relationship is much closer to linear, while the Wang–Schmugge model gives similar quasi-linear relationships at all frequencies. The interesting thing is that linear or quasi-linear relationships occurred at all frequencies in both model simulations and the plateau of $\Delta\epsilon$ is almost constant for different frequencies. The Dobson model gives a frequency-dependent slope and interception of $\Delta\epsilon$.

The difference between the Wang–Schmugge and the Dobson models lies in their theoretical basis. The Wang–Schmugge model is a linear mixture of the soil components' dielectric constants. It used the welting point to describe maximum bound water fraction, while the Dobson model used the double-layer model (Dobson et al. 1985) to describe the Debye-type relaxation of soil–water mixture. The Dobson model, however, is a linear mixture of the components'

dielectric constants to the power α. The power α is obtained from field measurements. From a theoretical point of view, the Dobson model better describes the dielectric constant at higher frequencies, for example, 37 GHz, because it accounts for the imaginary loss of microwave.

We used the Dobson model to calculate the dielectric constant at 37 GHz in Eqs. (10) and (11). Then, the PEED was simulated by the Q_p roughness model in Eq. (9). The linear relationships between PEED and soil moisture still occur, as shown in Fig. 8, though the interception and the plateau of $\Delta\epsilon$ are roughness dependent. The s/l is the RMS height divided by the correlation length, which represents the surface roughness: a smaller s/l value means a smoother surface. The slope of the relationships calculated for three different roughnesses slightly decreases with increasing roughness. This suggests that the fractional area of WSS and standing water as a linear function of the PEED [Eq. (2)] should depend on surface roughness. Because the terrain around the lake area is relatively smooth, we set the same roughness condition for all pixels (the white-numbered squares in Fig. 1).

The wind's influence on surface roughness is not significant, since 58% of the wind speed measured at the Boyang weather station near Poyang Lake is less than $2.0\,\mathrm{m\,s}^{-1}$ and 97% is less than $4.0\,\mathrm{m\,s}^{-1}$. That is because Poyang Lake and its floodplain are surrounded by mountains. The shape of the Poyang Lake floodplain looks like a quadrangle, with its northern edge facing to the northwest and its southern edge facing to the southeast. The eastern and western edges are almost parallel. The mean north–south distance is about 140 km, and the mean east–west distance is about 120 km. The lake has an irregular shape; it is located in the central floodplain and its eastern boundary is elongated in the same way as the eastern edge of the floodplain, with a north–south distance of about 100 km and an east–west distance of about 80 km. The
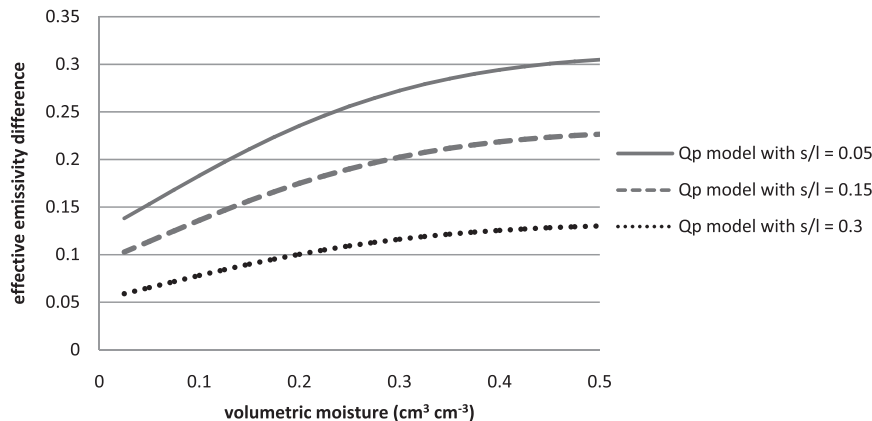
FIG. 8. Effective emissivity difference vs volumetric moisture at 37 GHz simulated from Q_p model and Dobson model of the soil dielectric constant.

lake connects to the Yangtze River to the north through a funnel-shaped area, with a wide mouth to the south and narrow head to the north. Thus, in the lake area, a north–south wind blows on most days. Only in July and August does the monsoon from the Indian Ocean force a south–north wind. The connecting funnel area yields a higher wind speed in the narrow head to the north and the wind speed decreases from north to south over the floodplain, after passing through this connecting area.

Thus, the largest mean wind speed occurs north of Poyang Lake, with an annual mean wind speed between 3 and 4 m s^{-1} from 1998 to 2007. In the center of the lake area, the mean wind speed is reduced to 2–3 m s^{-1}, while at the Nanchang meteorology station south of the lake, the mean wind speed is only 1.7 m s^{-1}.

To derive the model expressed by Eq. (2), the PEED of dry and water-saturated soil needs to be determined. According to Choudhury (1989), the PEED of dry soil is 0.091. Its surface roughness was calculated for an open water area by Choudhury with a corresponding $s/l =$ 0.175. The PEED of the paddy fields in Fig. 6, however, is close to 0.1 (the land surface temperature is assumed to be 270 K). This suggests that the land surface is much rougher than open water; thus, s/l is set as 0.25, with a corresponding $\Delta\epsilon_{\mathrm{dry}} = 0.068$. For completely water-saturated soil, we can assume that its PEED is the same as standing water, 0.21, given by Choudhury (1989). Equation (2) is then expressed as

$$f_{\mathrm{ws}} = (\Delta\epsilon - 0.068)/(0.21 - 0.068). \qquad (13)$$

d. Retrieved WSS and standing water area of Poyang Lake

Since we derive the vegetation transmission function using Eq. (12), PEED can be retrieved from noise-free

PDBT using Eq. (1), where T_s is obtained from noise-free vertical brightness temperature at 37 GHz [Eq. (4)] and the vegetation fractional area from noise-free NDVI [Eq. (5)]. The fractional area of WSS and standing water can then be calculated from the PEED using Eq. (13).

The WSS and standing water area enclosing Poyang Lake (white-numbered squares in Fig. 1) is calculated from 2001 to 2003 and compared with the Poyang Lake area from MODIS (with a spatial resolution of 250 m) and ASAR (with a spatial resolution of 30 m) data (Yésou et al. 2011, 2013), as shown in Table 2 (Yésou et al. 2011). The trend of our retrieved WSS and standing water area is close to the Poyang Lake area, as shown in Fig. 9. The RMSE of the retrieved WSS and standing water area is 361.22 km^2 or 17.74% of mean area during the same period of time. A wet and dry case of the pixel region centered at 29.0485°N, 116.0954°E is shown in Fig. 10. In the wet case of 4 July

TABLE 2. Comparison between lake area according to Yésou et al. (2011) and WSS and standing water area calculated from SSM/I 37 GHz.

| Date	Water extension from Yésou et al. (2011) (km^2)	Retrieved WSS and standing water area from SSM/I (km^2)
17 Jan 2001	1071.13	1308.71
12 Apr 2001	2186.69	1617.73
3 Jul 2001	2771.81	3072.36
16 Nov 2001	1669.44	947.683
9 Jan 2002	1174.31	1188.72
12 Apr 2002	1495	2173.18
21 Aug 2002	3212.81	3761.77
10 Nov 2002	2007	1287.61
25 Jan 2003	1751.09	1978.5
20 Jun 2003	2285.62	2319.19
25 Jul 2003	3305.69	3307.12
7 Nov 2003	1507.89	698.439
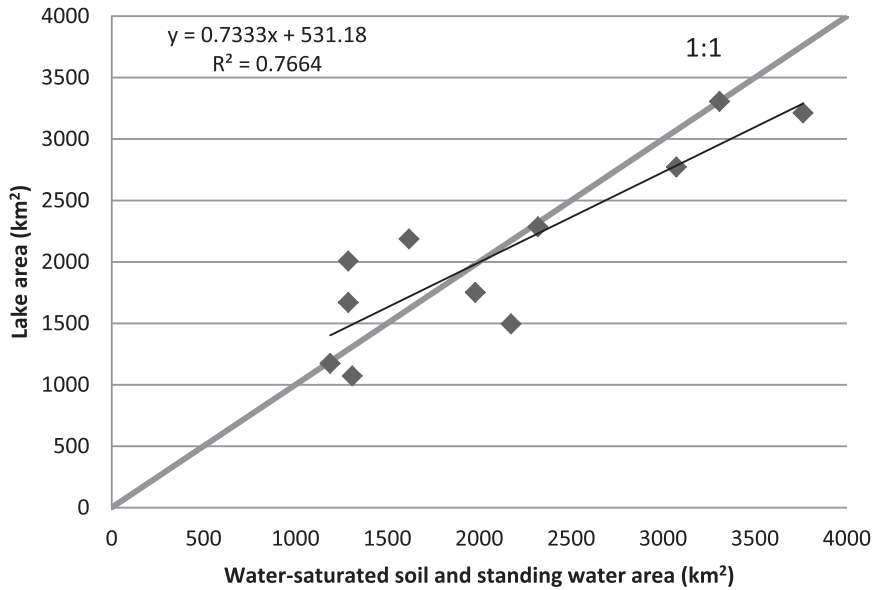
FIG. 9. Scatterplot of lake area estimated with MODIS and ASAR data by Yésou et al. (2011) and WSS and standing water area calculated from SSM/I 37 GHz.

2002, the fractional area of WSS and standing water, which is calculated from SSM/I (65.28%), is close to the fractional area of open water (58.81%) observed from MODIS NDVI images. However, in the dry case of 24 October 2002, the fractional area of WSS and standing water area (46.24%) is much larger than that of open water (21.85%) from NDVI. That is because the degraded lake area becomes wet land and is occupied by aquatic vegetation, mainly *Phragmites*. An optical sensor, like MODIS, cannot observe the standing water beneath the vegetation canopy, while a microwave radiometer can penetrate

FIG. 10. The (left) wet and (right) dry case of the five numbered pixels at Poyang Lake with corresponding NDVI images. The white rectangle inside the NDVI images is the area of the five numbered pixels of SSM/I 25-km EASE-Grid in the Poyang Lake area (Fig. 1) on 4 Jul and 24 Oct 2002. The upper part of the white rectangle represents the percentage (the numbers outside the parentheses) of the WSS and standing water area, which is calculated from SSM/I. The NDVI image is obtained from MOD09A1 with a spatial resolution of 500 m. The fractional open water area calculated from NDVI is shown in the parentheses.
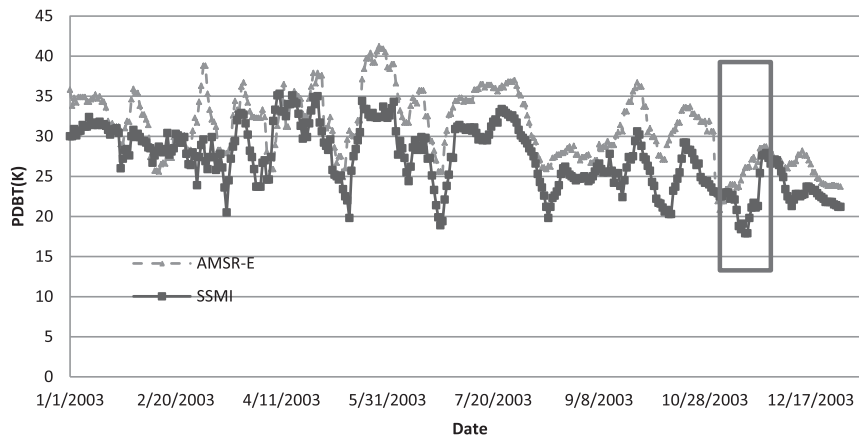
FIG. 11. Moving window–filtered PDBT (i.e., ΔT) data time series: comparison of AMSR-E and SSM/I measurements.

it. Thus, the WSS and standing water area is close to the total area of open water and the wetland vegetation.

The difference between our retrieved WSS and standing water area and the lake area from MODIS and ASAR data is mainly caused by three factors:

1) The study area is different. Yésou et al. (2011) focus on the Poyang Lake area, while our study area is $6250\,km^2$ and covers not only Poyang Lake, but also the wetland and cropland adjacent to Poyang Lake.

2) The observed features are different. The MODIS and ASAR capture the open water, while we observed the WSS and standing water. That means we cannot discriminate open water, flooded vegetation, and water-saturated soil using our model.

3) The temporal resolution is different. SSM/I data supply daily brightness temperature data, while the MODIS data used by Yésou et al. (2011) are 8-day composites and ASAR has a 35-day repeat orbit. Thus, near-daily monitoring is one of the advantages of using 37-GHz microwave radiometer data.

Another very important factor is the different impacts of vegetation on the three types of observation. The MODIS observations cannot penetrate under vegetation. In principle, ASAR can capture the backscatter from the water surface underneath the vegetation, but the scattering by vegetation is very strong. Our model takes the emittance of the WSS and standing water under vegetation cover into account.

After intersensor calibration, the retrieved sea surface temperature from these two datasets has a difference of less than 0.5 K. Though the brightness temperature data of the two radiometers have both been registered into the EASE-Grid system, the instantaneous field of view

(IFOV) of original data is rather different: $37\,km \times 28\,km$ for SSM/I and $14\,km \times 8\,km$ for AMSR-E. Thus, AMSR-E observes detailed changes in the lake area, especially during the dry season. The PDBT of SSM/I seems to be saturated earlier than AMSR-E, as shown by, for example, the peaks during May–October, since the AMSR-E observes a higher fractional WSS and standing water area in its IFOV than SSM/I. Taking the peaks in March and November in Fig. 11 as an example, the PDBT of SSM/I does not increase simultaneously with the AMSR-E, but 10 days later. In the period of 4–24 November 2003 (rectangle in Fig. 11), the SSM/I PDBT is about 5 K lower than AMSR-E, with the retrieved WSS and standing water area $345\,km^2$ lower than that from AMSR-E. The time series trend should be almost the same since two sensors both measure before sunrise. Over all comparison samples, our retrieved WSS and standing water area from SSM/I is closer to the Poyang Lake area from MODIS and SAR than that from AMSR-E, except for the samples in November 2003. Thus, there is a need for future work on the analysis of these two datasets.

To study the relationship between the soil water saturation conditions in the upstream catchment and the inundation pattern downstream, we retrieved the WSS and standing water area in the upper catchment. The upstream area of the Poyang Lake is indicated in Fig. 1 by the black-numbered EASE-Grid cells, and it includes the major tributary river systems from the western, southwestern, southeastern, and eastern directions. The downstream area is the lake area indicated by the white-numbered EASE-Grid cells.

The time series of the Poyang Lake area from 2001 to 2008 have similar fluctuations with the upstream WSS and standing water area (Fig. 12). For most periods, the Poyang Lake area increases with the upstream WSS and
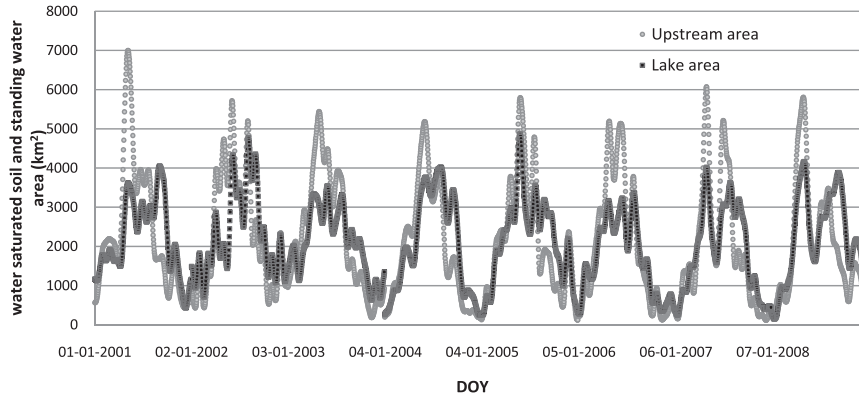
FIG. 12. Comparison between the upstream WSS and standing water area and that of the
Poyang Lake area.

standing water area. This is proven by the cross-correlation analysis between these two time series (Fig. 13): the maximum cross-correlation values from 2001 to 2008 are all higher than 0.5 and the time lag is no more than 5 days. The time lag indicates that the two time series are better correlated if shifted by this time lag relative to the other. In this case, it means that the increase of WSS and standing water area upstream will come earlier than that of the Poyang Lake area.

There are some peaks of the upstream WSS and standing water area that do not lead to the simultaneous increasing of lake area in Fig. 12. The reason is that the water source changes for the lake area. According to the long-term hydrological data in Poyang Lake, before July of each year, the water from upstream of the Poyang Lake floodplain (it is the subbasin of the Yangtze River basin) is the major source of lake. During this time, the lake area fluctuation is closely related with the WSS and standing water upstream in most years. There are some spikes in the upstream not leading to the same response in Poyang Lake, for example, at the end of April 2002 and 2003. That is because the surface runoff and streamflow is consumed by irrigation and other human activities before reaching the lake. From August of each year, the Poyang Lake area is supplied from both the upstream Poyang Lake floodplain and the Yangtze River. Thus, the asynchronism between upstream WSS and standing water area and the lake area becomes larger. For example, the spikes in the lake area in September 2001 and 2008 are probably caused by the water from the Yangtze River.

It is also interesting to observe that since 2003, the maximum cross-correlation value increased significantly. The major reason why the correlation coefficient changed after 2002 is that the water supplied by the Yangtze River changed since building the Three Gorges Dam. The Three Gorges Dam was closed to store water

from November 2002 to 2006. The water flow from the Yangtze River to Poyang Lake is limited to the period from August to September, that is, the flooding season of the Yangtze River. Thus, the water source of Poyang Lake is mainly from the upstream catchment, and the correlation coefficients increase from 2003 to 2006. Since 2007, the dam stopped storing water and released the streamflow as usual. An obvious decrease then occurs in the coefficients of Fig. 13. This again proves that the water supplement from the Yangtze River will significantly influence the lake changes since August.

5. Conclusions

We used a simplified radiative transfer model and linear model to retrieve the fractional area of water-saturated soil (WSS) and standing water from the polarization difference brightness temperature (PDBT) at 37 GHz. The moving filter is first used to fill the observation gaps of the PDBT time series. Noise-free daily PDBT, vertical brightness temperature (BT), and NDVI
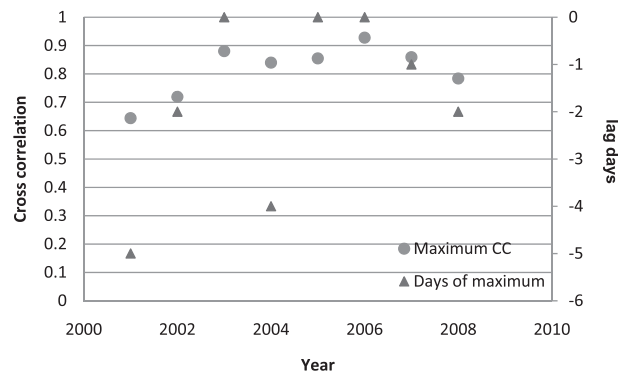

FIG. 13. Max cross-correlation values between time series of upstream WSS and standing water area and that of the Poyang Lake area from 2001 to 2008 and the days that max time lag occurs.

are derived from the Harmonic Analysis of Time Series (HANTS) algorithm of their raw data time series. The vegetation transmission function is obtained from the regression between NDVI and its dependent variable PDBT for flooded paddy fields, under the assumption that the land surface temperature and PEED of the flooded rice is constant during its growing season. The quasi-linear relationship between the PEED and fractional area of WSS and standing water exists no matter what the frequencies are. This indicates that the regional water-storage capacity can be derived from PDBT observations of other frequencies. The retrieved WSS and standing water area in the Poyang Lake region shows a good fit with the lake area from the MODIS and SAR data. Our method seems to provide satisfactory estimates of the water-storage capacity of the upper catchment of the Poyang Lake, and as such, it is a useful early indicator of flooding events in the lake area.

REFERENCES

Alfieri, S. M., F. De Lorenzi, and M. Menenti, 2013: Mapping air temperature using time series analysis of LST: The SINTESI approach. *Nonlinear Processes Geophys.,* **20,** 513–527, doi:10.5194/npg-20-513-2013.

Armstrong, R., K. Knowles, M. Brodzik, and M. A. Hardman, 1998: DMSP SSM/I–SSMIS Pathfinder daily EASE-Grid brightness temperatures, version 2. National Snow and Ice Data Center, Boulder, CO, digital media. [Available online at http://nsidc.org/data/nsidc-0032.]

Brodzik, M., and K. Knowles, cited 2002: EASE-Grid: A versatile set of equal-area projections and grids. Discrete global grids: A web book, National Center for Geographic Information and Analysis, Santa Barbara, CA. [Available online at www.ncgia.ucsb.edu/globalgrids-book/ease_grid/.]

Calvet, J. C., J. P. Wigneron, A. Chanzy, S. Raju, and L. Laguerre, 1995: Microwave dielectric properties of a silt-loam at high frequencies. *IEEE Trans. Geosci. Remote Sens.,* **33,** 634–642, doi:10.1109/36.387579.

Choudhury, B. J., 1989: Monitoring global land surface using *Nimbus-7* 37 GHz data: Theory and examples. *Int. J. Remote Sens.,* **10,** 1579–1605, doi:10.1080/01431168908903993.

——, 1991: Passive microwave remote sensing contribution to hydrological variables. *Surv. Geophys.,* **12,** 63–84, doi:10.1007/BF01903412.

——, and C. J. Tucker, 1987: Monitoring global vegetation using *Nimbus-7* 37 GHz data: Some empirical relations. *Int. J. Remote Sens.,* **8,** 1085–1090, doi:10.1080/01431168708954754.

——, J. R. Wang, A. Y. Hsu, and Y. L. Chien, 1990: Simulated and observed 37 GHz emission over Africa. *Int. J. Remote Sens.,* **11,** 1837–1868, doi:10.1080/01431169008955133.

De Ridder, K., 2000: Quantitative estimation of skin soil moisture with the special sensor microwave/imager. *Bound.-Layer Meteor.,* **96,** 421–432, doi:10.1023/A:1002668624711.

Dobson, M. C., F. T. Ulaby, M. T. Hallikainen, and M. A. Elrayes, 1985: Microwave dielectric behavior of wet soil. 2. Dielectric mixing models. *IEEE Trans. Geosci. Remote Sens.,* **23,** 35–46, doi:10.1109/TGRS.1985.289498.

Gao, H. L., E. F. Wood, M. Drusch, W. Crow, and T. J. Jackson, 2004: Using a microwave emission model to estimate soil moisture from ESTAR observations during SGP99. *J. Hydrometeor.,* **5,** 49–63, doi:10.1175/1525-7541(2004)005<0049:UAMEMT>2.0.CO;2.

Hamilton, S. K., S. J. Sippel, and J. M. Melack, 1996: Inundation patterns in the Pantanal wetland of South America determined from passive microwave remote sensing. *Arch. Hydrobiol.,* **137,** 1–23.

Hollinger, J. P., J. L. Peirce, and G. A. Poe, 1990: SSM/I instrument evaluation. *IEEE Trans. Geosci. Remote Sens.,* **28,** 781–790, doi:10.1109/36.58964.

Holmes, T. R. H., R. A. M. De Jeu, M. Owe, and A. J. Dolman, 2009: Land surface temperature from Ka band (37 GHz) passive microwave observations. *J. Geophys. Res.,* **114,** D04113, doi:10.1029/2008JD010257.

Huber, C., and Coauthors, 2013: Twelve year of water resource monitoring over Yangtze middle reaches exploiting Dragon time series and field measurements. *Proc. Dragon 2 Final Results and Dragon 3 Kick-Off Symp.,* Beijing, China, Ministry of Science and Technology of China and European Space Agency, CD-ROM.

Jia, L., H. Shang, G. Hu, and M. Menenti, 2011: Phenological response of vegetation to upstream river flow in the Heihe Rive basin by time series analysis of MODIS data. *Hydrol. Earth Syst. Sci.,* **15,** 1047–1064, doi:10.5194/hess-15-1047-2011.

Julien, Y., J. A. Sobrino, and W. Verhoef, 2006: Changes in land surface temperatures and NDVI values over Europe between 1982 and 1999. *Remote Sens. Environ.,* **103,** 43–55, doi:10.1016/j.rse.2006.03.011.

Kirdiashev, K. P., A. A. Chucklantsev, and A. Shutko, 1979: Microwave radiation of the earth's surface in the presence of vegetation cover. *Radiotecknica,* **24,** 256–264.

Menenti, M., S. Azzali, W. Verhoef, and R. van Swol, 1993: Mapping agroecological zones and time lag in vegetation growth by means of Fourier analysis of time series of NDVI images. *Adv. Space Res.,* **13,** 233–237, doi:10.1016/0273-1177(93)90550-U.

——, L. Jia, S. Azzali, G. J. Roerink, M. Gonzalez-Loyarte, S. Leguizamon, and W. Verhoef, 2010: Analysis of vegetation response to climate variability using extended time series of multispectral satellite images. *Remote Sensing Optical Observations of Vegetation Properties,* F. Maselli, M. Meneti, and P. A. Brivio, Eds., Research Signpost, 131–164.

Moody, A., and D. M. Johnson, 2001: Land-surface phenologies from AVHRR using the discrete Fourier transform. *Remote Sens. Environ.,* **75,** 305–323, doi:10.1016/S0034-4257(00)00175-9.

Poe, G. A., 1990: Optimum interpolation of imaging microwave radiometer data. *IEEE Trans. Geosci. Remote Sens.,* **28,** 800–810, doi:10.1109/36.58966.

Roerink, G. J., M. Menenti, and W. Verhoef, 2000: Reconstructing cloudfree NDVI composites using Fourier analysis of time series. *Int. J. Remote Sens.,* **21,** 1911–1917, doi:10.1080/014311600209814.

——, ——, W. Soepboer, and Z. Su, 2003: Assessment of climate impact on vegetation dynamics by using remote sensing. *Phys. Chem. Earth Parts ABC,* **28,** 103–109, doi:10.1016/S1474-7065(03)00011-1.

Shi, J. C., L. M. Jiang, L. X. Zhang, K. S. Chen, J. P. Wigneron, and A. Chanzy, 2005: A parameterized multifrequency-polarization surface emission model. *IEEE Trans. Geosci. Remote Sens.,* **43,** 2831–2841, doi:10.1109/TGRS.2005.857902.

——, T. Jackson, J. Tao, J. Du, R. Bindlish, L. Lu, and K. S. Chen, 2008: Microwave vegetation indices for short vegetation covers from satellite passive microwave sensor AMSR-E. *Remote Sens. Environ.,* **112,** 4285–4300, doi:10.1016/j.rse.2008.07.015.

Sippel, S. J., S. K. Hamilton, J. M. Melack, and B. J. Choudhury, 1994: Determination of inundation area in the Amazon River floodplain using the SMMR 37 GHz polarization difference. *Remote Sens. Environ.,* **48,** 70–76, doi:10.1016/0034-4257(94)90115-5.

——, ——, ——, and E. M. M. Novo, 1998: Passive microwave observations of inundation area and the area/stage relation in the Amazon River floodplain. *Int. J. Remote Sens.,* **19,** 3055–3074, doi:10.1080/014311698214181.

van de Griend, A. A., and M. Owe, 1993: Determination of microwave vegetation optical depth and single scattering albedo from large-scale soil-moisture and Nimbus SMMR satellite-observations. *Int. J. Remote Sens.,* **14,** 1875–1886, doi:10.1080/01431169308954009.

Verhoef, W., 1996: Application of Harmonic Analysis of NDVI Time Series (HANTS). *Fourier Analysis of Temporal NDVI in the Southern African and American Continents,* S. Azzali and M. Menenti, Eds., Netherlands Remote Sensing Board, 19–24.

Wang, J. R., and T. J. Schmugge, 1980: An empirical-model for the complex dielectric permittivity of soils as a function of water-content. *IEEE Trans. Geosci. Remote Sens.,* **18,** 288–295, doi:10.1109/TGRS.1980.350304.

Wen, J., Z. B. Su, and Y. M. Ma, 2003: Determination of land surface temperature and soil moisture from Tropical Rainfall Measuring Mission/Microwave Imager remote sensing data. *J. Geophys. Res.,* **108,** 4038, doi:10.1029/2002JD002176.

Wigneron, J. P., Y. Kerr, A. Chanzy, and Y. Q. Jin, 1993: Inversion of surface parameters from passive microwave measurements over a soybean field. *Remote Sens. Environ.,* **46,** 61–72, doi:10.1016/0034-4257(93)90032-S.

Yésou, H., and Coauthors, 2011: Nine years of water resources monitoring over the middle reaches of the Yangtze River, with ENVISAT, MODIS, Beijing-1 time series, Altimetric data and field measurements. *Lakes Reservoirs,* **16,** 231–247, doi:10.1111/j.1440-1770.2011.00481.x.

——, C. Huber, H. Shifeng, L. Xijun, and D.-R. Sylviane, 2013: Chinese lakes behaviours in the framework of the meteorology and water management practices: EO based monitoring lessons. *Proc. Living Planet Symp. 2013,* Edinburgh, United Kingdom, ESA, CD-ROM.

Zhao, L., and Coauthors, 2013: Spatiotemporal analysis of soil moisture observations within a Tibetan mesoscale area and its implication to regional soil moisture measurements. *J. Hydrol.,* **482,** 92–104, doi:10.1016/j.jhydrol.2012.12.033.